# Contents

# Verification and Validation

Computer simulations are in many engineering applications a cost-efficient way for conducting design and performance optimalization of physical problems. However, trusting blindly numbers generated from a computer code can prove to be naive. It doesn't take a lot of coding experience before one realizes the many things that can brake down and produce unwanted or unexpected results. Therefore, *credability* of computational results are essential, meaning the simulation is worthy of belief or confidence [25]. *Verification and validation* (V&V) is the main approach for assessing and the reliability of computational simulations [37]. A thorough discussion of (V&V) concepts and terminology during the last century can be found in [25]. In this thesis, the definitions provided by the *American Society of Mechanical Engineers guide for Verification and Validation in Computational Solid Mechanics* [34] are followed:

**Definition 1.1.** Verification: The process of determining that a computational model accurately represents the underlying mathematical model and its solution.

**Definition 1.2.** Validation: The process of determining the degree to which a model is an accurate representation of the real world from the perspective of the intended uses of the model.

Simplified *verification* considers if one solves the equations right, while *validation* is checking if one solves the right equations for the given problem [31]. To test a computational code for all possible parameters, conditions and applications are simply too time consuming. Verification and validation are therefore ongoing processes, with no clear boundary of completeness unless additional requirements are specified [31]. The goal of this chapter is to verify our implementations using the method of manufactured solution (MMS), addressing validation in a subsequent chapter.

## 1.1 Verification of Code

Within scientific computing a mathematical model is often the baseline for simulations of a particular problem of interest. For scientists exploring physical phenomena, the mathematical model is often on the form of systems of partial differential equations (PDEs). A computer program therefore must evaluate mathematical identities such a differential operators and functions in order to produce accurate

solutions of the governing PDEs. Through verification of code, the ultimate goal is to ensure a computer program truly represents the mathematical model. To accumulate sufficient evidence that a mathematical model is solved correctly by a computer code, it must excel within predefined criteria. If the acceptance criterion is not satisfied, a coding mistake is suspected. Should the code pass the preset criteria, the code is considered verified. Of the different classes of test found in [31], *Order-of-accuracy* (OAA) is regarded as the most rigorous acceptance criterion for verification [33, 31, 5]. The method tests if the discretization error $E$ is reduced in coordinance with the *formal order of accuracy* expected from the numerical scheme. The formal order of accuracy is defined to be the theoretical rate at which the truncation error of a numerical scheme is expected to reduce. The *observed order of accuracy* is the actual rate produced by the numerical solution. For order of convergence tests, the code is assumed to be verified if the observed discretization error is proportional to the formal order of accuracy.By monitoring the dicretization error $E$ by spatial and temporal refinements, OAA tests assumes the error $E$ can be expressed as,

$$E = C\Delta t^p + D\Delta x^l$$

where C and D are is constants, $\Delta t$ and $\Delta x$ represents the spatial and temporal resolution, while $p$ and $l$ is the observed order of accuracy of the numerical scheme. If $\Delta x$is small compared to $\Delta t$, the spatial discretization error can be neglected, and we can use that to find $l$, which is the observed order of convergence for the temporal discretization error. To calculate the error $E$, an exact/reference solution is needed which rarely exist for complex mathematical models. The next subsection presents an efficient method for generating such solutions.

### 1.1.1 Method of manufactured solution

The basis of a convergence test is how to find an exact/reference solution, in order to compute the discretization error $E$. However solutions of PDEs are limited, and often simplifications of the original problem are needed to produce analytically solutions. *The method of manufactured solutions* provides a simple yet robust way of making analytic solutions for PDEs. Let a partial differential equation of interest be on the form

$$\mathbf{L}(\mathbf{u}) = \mathbf{f}$$

Here $\mathbf{L}$ is a differential operator, $\mathbf{u}$ is variable the of interest, and $\mathbf{f}$ is some sourceterm. In MMS, one first manufactures a solution $\mathbf{u}$ for the given problem. In general, the choice of $\mathbf{u}$ will not satisfy the governing equations, producing a sourceterm $\mathbf{f}$ after differentiation by $\mathbf{L}$. The produced source term will cancel any imbalance formed by the manufactured solution $\mathbf{u}$ of the original problem. Therefore, the manufactured solution can be constructed without any physical reasoning, proving code verificaion as a purely a mathematical exercise were our only interest is to verify the solution [30].

If the MMS is not chosen properly the test will not work, therfore some guidelines for rigirous verification have been proposed in [5, 33, 30].

- The manufactured solution (MS), should be composed of smooth analytic functions such as exponential, trigonometric, or polynomials.
- The MS should should have sufficient number of derivatives, exercising all terms and derivatives of the PDEs.

To deeply verify the robustness of the method of manufactured solution, a report regarding code verification by MMS for the time-dependent Navier-Stokes equation was published by Salari and Knupp [33]. To prove its robustness the authors deliberate implemented code errors in a verified Navier-Stokes solver by MMS presented in the report. In total 21 blind testcases where implemented, where different approaches of verification frameworks were tested. Of these, 10 coding mistakes that reduced the observed order-of-accuracy was implemented. The MMS captured all coding mistakes, except one. This mistake would, accordingly to the co-author, been captured if his guidelines for conducting MMS had been followed.

In general, computing the source term f can be quite challenging and error prone. Therefore, symbolic computation of the sourcterm is advantigous to overcome mistakes which can easily occur when calulating by hand. For construction of the sourceterm $\mathbf{f}$, the Unified Form Language (UFL) [**?**] provided in FEniCS Project will be used. COMPUTE VV HERE

### 1.1.2 Comment on verification of the fluid-structure interaction solver by MMS

In general the MMS does not need to match any physical processes. However, when considering multiphysics problems, such as FSI, the equations has to meet the mathematical criteria from **??**

*Let $\hat{\mathbf{v}}_s, \hat{\mathbf{v}}_f$ be the structure and fluid velocity, and let $\sigma_s$, $\sigma_f$ be the Cauchy stress tensor for the structure and fluid respectively. Let $\mathbf{n}_i$ be the normal vector pointing out of the domain $i$. We then have the following interface boundary conditions,*

1. Kinematic boundary condition $\hat{\mathbf{v}}_s = \hat{\mathbf{v}}_f$, enforced strongly by a continious velocity field in the fluid and solid domain.
2. Dynamic boundary condition $\sigma_s \cdot \mathbf{n}_s = \sigma_f \cdot \mathbf{n}_f$, enforced weakly by omitting the boundary integrals from the weak formulation in problem.

The choice of a MMS is therefore not trivial, as it must fulfill condition 1 and 2, in addition to the divergence-free condition in the fluid, and avoiding cancellation of the ALE-convective term $\frac{\partial \hat{T}_f}{\partial t}$. The construction of a MMS for a monolithic FSI problem is therefore out of the scope of this thesis. The struggle is reflected of the abscence of research, regarding MMS for coupled FSI solvers in the litterature. The challenge is often disregarded, such as [35], where the verification process is

conducted on the fluid and structure solver separately. Instead, the correctness of the coupling is evaluated by the code validation. The approach clearly ease the process, assuming verification of each codeblock is "sufficient" to declare the code verified. In this thesis, the approach found in [35] was followed, but it must be stressed that solving each problem individually is not true verification, in reference to a monolithic approach where the problems are solved at the same time.

## 1.2 Validation of Code

Through *verification*, one can assure that a scientific code evaluate mathematical model correctly. However, accuracy is unnecessary if the model fails to serve as an accurate representation of the physical problem of interest. By definition 1.2, *Validation* is the act of demonstrating that a mathematical model is applicable for its intended use with a certain degree of accuracy. That is, a mathematical model is validated if it meets some predefined criteria within a specific context. Validation is therefore not intended to portray the model as an absolute truth, nor the best model available [32]. In computational science, validation is conducted by comparing numerical results against existing experimental data. The design of validation experiments vary by the motivation of the of their creators, where validated experiments for computational science can be divided into three groups[37]: (1) To improve fundamental understanding of a physical process, (2) Discovery or enhancement of mathematical models of well known physical processes, (3) to conclude the reliability and performance of systems. The assessment of comparison between numerical results and experimental data, makes *validation* assess a wide range of issuses [37]. Is the experiment relevant, and conducted correctly in accordinance with prescribed parameters? What about the measurement uncertainty of reference experimental data? These issues must be addressed in order to raise sufficient confidence that the mathematical model is credible for its intended use.

Validation of FSI is demanding due to the number of building blocks composing the full problem. For *interface-tracking* methods such as the ALE-method, validation is not only related to the physical aspcets of the model. Even if the fluid and structure models excel well within predefined criteria, the non-physical nature of mesh moving models have proven to affect the numerical solution [47]. At first glance, this effect is surprising as mesh moving models simply describe the evolution of fluid mesh cells from the moving interface. However, each model distributes the fluid cells differently, which in turn may have an important effect when conducting mathematical operations such as gradients.

The numerical benchmark presented in [15] has been chosen for validation of the *One-step* $\theta$ scheme from chapter 3. The benchmark has been widely accepted throughout the fluid-structure interaction community as a rigid validation benchmark [47, 49, 42, 11]. This is mainly due to the diversity of tests included, challenging all the main components of a fluid-structure interaction scheme. The benchmark is based on the *von Kármán vortex street* [45], where a cylinder is placed off center in a channel. In [15], an additional elastic flag is placed behind the cylinder, see Figure 4.1

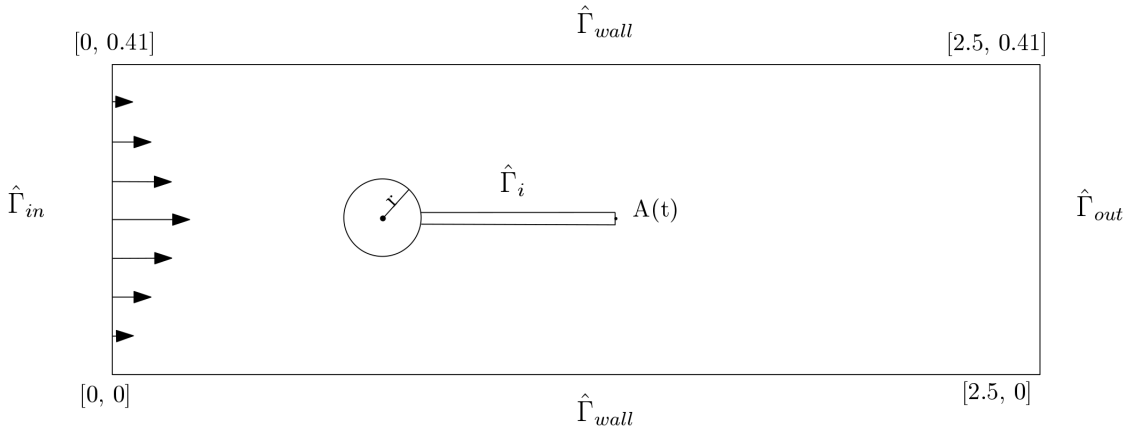


Figure 1.1: Computational domain of the validation benchmark

The benchmark is divided into three main test branches, further divided into three different problems with increasing difficulty. In the first branch, the fluid solver is tested for a series of different flow profiles. The second branch considers the structure solver, regarding bending of the elastic flag. And the final branch concerns validation a full fluid-structure interaction problem. Several quantites for comparion are presented in [15] for validation purposes:

- The position (x,y) of point A(t) as the elastic flag undergoes deformation.
- Drag and lift forces exerted on of the whole interior geometry in contact with the fluid, consisting of the rigid circle and the elastic beam.

$$(F_D, F_L) = \int_\Gamma \sigma \cdot \mathbf{n} dS$$

All branches pose both steady state and periodic solutions. For the steady state solutions, the quantity of interest will be calculated for the last time step. For the periodic solutions, the amplitude and mean values for the time dependent quantity are calculated from the last period of oscillations,

$$\text{mean} = \frac{1}{2}\text{max} + \text{min} \tag{1.1}$$

$$\text{amplitude} = \frac{1}{2}\text{max - min} \tag{1.2}$$

In [15], all steady state solutions seems to be calulated by solving a steady state equation since time-step are only reported for the periodic solutions. In this thesis, all problems in [15] are calculated by time integration. The main motivation is based upon that any given numerical errors regarding time integration will be intercepted at an earlier stage for a simpler problem. Therefore, the choice of time step is chosen such that reasonable accuracy of the reference solution is attained.
In the following section, an overview of each branch together with numerical results will be presented. A discussion of the results are given at the end of each simulation brancht. For each table, the relative error of the finest spatial and temporal refinement compared to the reference solution is reported in [15]

### 1.2.1 Validation of fluid solver

The first test branch conserns the fluid solver for low Reynold-number regime. Two approaches for the validation are given in [15]. The first approach considers the setup as a fluid-structure interaction problem, by setting the elastic flag close to rigid by manipulation of the structure parameters. In the second approach, the flag is set fully rigid and considered a purely flow problem. By this proposal, no deformation of the fluid domain occurs, reducing the fluid variation formulation to its original form,

$$\begin{aligned}\Big(\frac{\partial \hat{\mathbf{v}}_f}{\partial t},\ \hat{\boldsymbol{\psi}}^u\Big)_{\hat{\Omega}_f} + \big((\hat{\mathbf{v}}_f \cdot \hat{\nabla})\hat{\mathbf{v}}_f,\ \hat{\boldsymbol{\psi}}^u\big)_{\hat{\Omega}_f} - \big(\hat{\sigma},\ \hat{\nabla}\hat{\boldsymbol{\psi}}^u\big)_{\hat{\Omega}_f} - \big(\rho_f \mathbf{f}_f,\ \hat{\boldsymbol{\psi}}^u\big)_{\hat{\Omega}_f} &= 0 \\ \big(\nabla \cdot \hat{\mathbf{v}}_f),\ \hat{\boldsymbol{\psi}}^p\big)_{\hat{\Omega}_f} &= 0\end{aligned}$$

The latter approach is chosen for this thesis, as only the variational formulation for the fluid is tested and removes any influence of the structure and mesh extrapolation discretization.

| parameter | CFD-1 | CFD-2 | CFD-3 |
|---|---|---|---|
| $\rho^f[10^3 \frac{kg}{m^3}]$ | 1 | 1 | 1 |
| $\nu^f[10^{-3} \frac{m^2}{s}]$ | 1 | 1 | 1 |
| U | 0.2 | 1 | 2 |
| Re | 20 | 100 | 200 |

Table 1.1: Fluid sub-problem parameters

The validation of the fluid solver is divided into three sub-problems; CFD-1, CFD-2, and CFD-3, each with different fluid parameters shown in Table 1.1 While CFD-1 and CFD-2 yields steady state solutions, CFD-3 is a periodic solution. A parabolic velocity profile on the form,

$$v_f(0, y) = 1.5U \frac{(H - y)y}{(\frac{H}{2})^2}$$

is set on the left channel inflow. H is the height of the channel, while the parameter U is set differently to each problem to induce different inlet flow profiles. At the right channel outflow, the pressure is set to $p = 0$. No-slip boundary conditions for the fluid are enforced on the channel walls, and on the inner geometry consisting of the circle and the elastic flag. The validation of the fluid solver is based on the evaluation of drag and lift forces on the inner geometry, in comparison with a reference solution. A spatial and temporal convergence study is conducted on all sub-cases The following tables presents the numerical results for each sub-problem.

**Results**

Table 1.2, 1.3, and 1.4 shows the numerical solution of each sub, CFD-1, CFD-2, and CFD-3. Each sub-problem is evaluated on for four different mesh with increasing resolution. For the numerical solution of CFD-3 in Table 4.4, additional temporal and spatial refinement studies are conducted. Figure 4.1 shows the evaluation of lift and drag for the finest spatial and temporal resolution, while Figure 4.3 shows a visual representation of the fluid flow through the channel.

| $\Delta t = 0.1 \ \ \theta = 1.0$ | | | |
|---|---|---|---|
| nel | ndof | Drag | Lift |
| 1438 | 6881 | 13.60 | 1.089 |
| 2899 | 13648 | 14.05 | 1.126 |
| 7501 | 34657 | 14.17 | 1.109 |
| 19365 | 88520 | 14.20 | 1.119 |
| Reference | | 14.29 | 1.119 |
| Error | | 0.006 % | 0.00 % |

Table 1.2: CFD-1 results, lift and drag evaluated at the inner geometry surface for increasing spatial refinement. The error is computed as the relative error from the highest mesh resolution against the reference solution.

| $\Delta t = 0.01$ $\theta = 1.0$ | | | |
|---|---|---|---|
| nel | ndof | Drag | Lift |
| 1438 | 6881 (P2-P1) | 126.0 | 8.62 |
| 2899 | 13648 (P2-P1) | 131.8 | 10.89 |
| 7501 | 34657 (P2-P1) | 135.1 | 10.48 |
| 19365 | 88520(P2-P1) | 135.7 | 10.55 |
| Reference | | 136.7 | 10.53 |
| Error | | 0.007 % | 0.001 % |

Table 1.3: CFD-2 results, lift and drag evaluated at the inner geometry surface for increasing spatial refinement. The error is computed as the relative error from the highest mesh resolution against the reference solution.

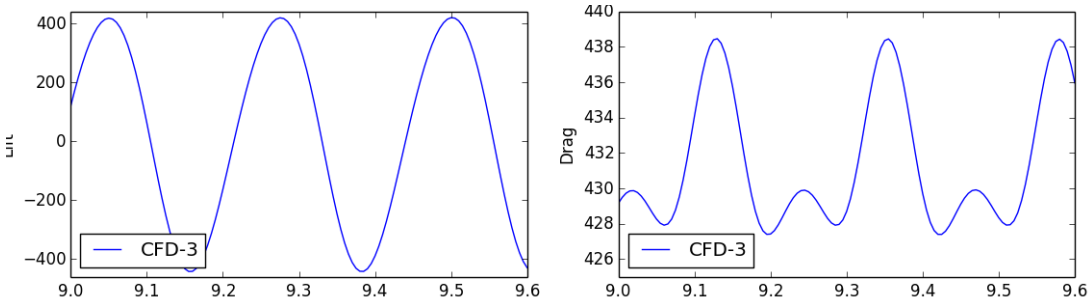


Figure 1.2: CFD-3, lift and drag forces at time t = [9, 9.6].

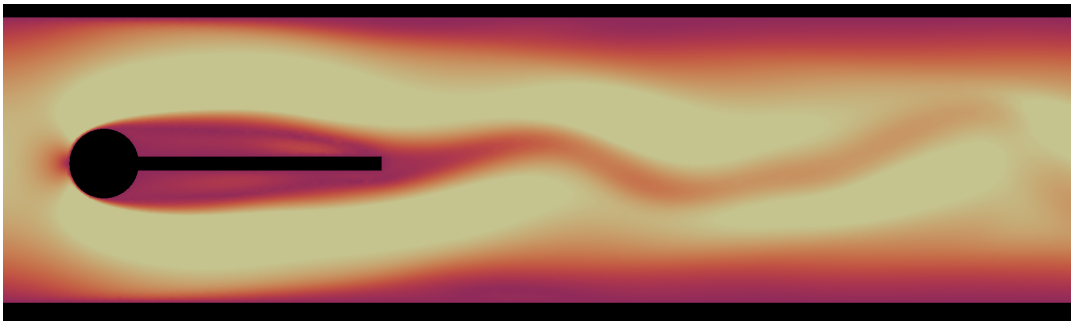

Figure 1.3: CFD-3, flow visualization of velocity time t = 9s.

| $\Delta t = 0.01$ $\theta = 0.5$ | | | |
|---|---|---|---|
| nel | ndof | Drag | Lift |
| 1438 | 6881 (P2-P1) | 417.23 +/- 0.0217 | -249.21 +/- 0.32 |
| | 16474 (P3-P2) | 414.86 ± 5.6282 | -7.458 ± 444.07 |
| 2899 | 13648 (P2-P1) | 408.50 ± 4.3029 | -19.731 ± 373.45 |
| | 32853 (P3-P2) | 432.86 ± 5.5025 | -9.686 ± 431.28 |
| 7501 | 34657 (P2-P1) | 431.57 ± 5.2627 | -12.497 ± 429.76 |
| | 83955 (P3-P2) | 438.20 ± 5.5994 | -11.595 ± 438.00 |
| 19365 | 88520 (P2-P1) | 435.43 ± 5.4133 | -11.545 ± 438.89 |
| | 215219 (P3-P2) | 438.80 ± 5.6290 | -11.158 ± 439.23 |
| Reference | | 439.95 ± 5.6183 | -11.893 ± 437.81 |
| Error | | 0.002 % ± 0.001 % | 0.061 % ± 0.003% |
| $\Delta t = 0.005$ $\theta = 0.5$ | | | |
| nel | ndof | Drag | Lift |
| 1438 | 6881 (P2-P1) | 417.24 ± 0.0084 | -249.386 ± 0.1345 |
| 1438 | 16474 (P3-P2) | 414.90 ± 5.7319 | -8.467 ± 443.45 |
| 1438 | 13648 (P2-P1) | 408.27 ± 4.0192 | -18.981 ± 363.84 |
| 2899 | 32853 (P3-P2) | 432.90 ± 5.5333 | -11.382 ± 430.60 |
| 1438 | 34657 (P2-P1) | 431.59 ±5.2979 | -13.644 ± 429.68 |
| 7501 | 83955 (P3-P2) | 438.23 ± 5.6393 | -12.917 ± 437.78 |
| 1438 | 88520 (P2-P1) | 435.46 ± 5.4579 | -13.190 ± 438.05 |
| 19365 | 215219 (P3-P2) | 438.84 ± 5.6576 | -12.786 ± 438.36 |
| Reference | | 439.95 ± 5.6183 | -11.893 ± 437.81 |
| Error | | 0.002 % ± 0.006 % | 0.075 % ± 0.001% |

Table 1.4: CFD-3 results, lift and drag evaluated at the inner geometry surface. A spatial refinement study is conducted for increasing mesh resolution and two different finite element pairs. The relative error is computed from the solution of the highest mesh resolution, against the reference solution.

**Discussion**

The numerical solutions of CFD-1 in Figure 4.2 shows convergence against the reference solution. Choosing P2-P1 elements together with a fully implicit scheme $\theta = 1$, a relative error of 0.006% for lift, and 0% for drag is attained. For the numerical solution of CFD-2 presented in Figure 4.3, the same observations apply. The second order Crank–Nicolson scheme $\theta = 0.5$ was investigated for CFD-1 and CFD-2, however only improving the results of order $10^{-6}$ for both lift and drag. For the periodic problem CFD-3, the choice of P2-P1 elements with a fully implicit time-stepping scheme proved insufficient for capturing the expected periodic solution. By Crank–Nicolson time-stepping scheme $\theta = 0.5$, the periodic solution was attained. Since the choice of finite-element pair is not reported in the original work, both P3-P2 and P2-P1 element pairs for fluid and pressure respectively was compared in combination with spatial mesh refinement. From Table 4.3, a relative error $< 0.08\%$ of the mean and amplitude for lift and drag is attained. The choice P3-P2 element pair is eminent to achieve reasonable results for the first and second mesh regardless of time step. However, the third and fourth mesh resolution shows close resemblance with the reference solution, independent of finite-element pair. On basis of the presented results, the fluid solver is validated in accordance with the proposed benchmark.

### 1.2.2 Validation of solid solver

The validation of the solid solver is conducted on a rectangular domain, representing the elastic structure in Figure 1.1. The structure is submitted to a gravitational for $\mathbf{g} = (0, g)$, while beeing fixed to a fictional wall on the left side of the domain. The validation of the solid solver is based on comparison of the deflection of point $A(t) = [A_x(t), A_y(t)]$, conducted on three refined mesh, where the number of finite elements are chosen in close resemblance with the original work in [15]. A simple investigation of different finite-element pairs, suggest that P3-P3 elements where used for making the reference solution. In this study, lower order finite-element pair was included by the motivation of shorter simulation time while retaining solution accuracy. While computational time is not a major concern for the solid solver, the study is important for potentially reducing the computational time for the final validation branch

| parameter | CSM 1 | CSM 2 | CSM 3 |
|---|---|---|---|
| $\rho^s[10^3 \frac{kg}{m^3}]$ | 1 | 1 | 1 |
| $\nu^s$ | 0.4 | 0.4 | 0.4 |
| $\mu^s[10^6]$ | 0.5 | 2.0 | 0.5 |
| $g\frac{m}{s^2}]$ | 2.0 | 2.0 | 2.0 |

Table 1.5: Solid sub-problem parameters

### Results

The numerical results for CSM-1, CSM-2, and CSM-3 are presented in table Table 1.6, 1.7, 1.8, and 1.9. For the steady state sub-problems CSM-1 and CSM-2, a spatial convergence study is conducted by mesh refinement with three different finite-element pairs. For the periodic CSM-3 problem, an additional temporal study was conducted for two different time steps. In Figure 1.4, a visualization of CSM-3 is provided for three different time steps. Finally, Figure 1.5 shows the displacement vector components, comparing all finite-element pairs for the finest mesh resolution.

| $\Delta t = 0.1 \;\; \theta = 1.0$ | | | |
|---|---|---|---|
| nel | ndof | ux of A [x $10^{-3}$] | uy of A [x $10^{-3}$] |
| 319 | 832 P1-P1 | -5.278 | -56.6 |
| | 2936 P2-P2 | -7.056 | -65.4 |
| | 6316 P3-P3 | -7.064 | -65.5 |
| 1365 | 3140 P1-P1 | -6.385 | -62.2 |
| | 11736 P2-P2 | -7.075 | -65.5 |
| | 25792 P3-P3 | -7.083 | -65.5 |
| 5143 | 11084 P1-P1 | -6.905 | -64.7 |
| | 42736 P2-P2 | -7.083 | -65.4 |
| | 94960 P3-P3 | -7.085 | -65.5 |
| Reference | | -7.187 | -66.1 |
| Error | | 1.41 % | 0.8 % |

Table 1.6: CSM-1, deformation components of A(t) for $\Delta t = 0.1$ and increasing spatial refinement. The error is computed as the relative error from the highest mesh resolution against the reference solution.

| $\Delta t = 0.05 \;\; \theta = 1.0$ | | | |
|---|---|---|---|
| nel | ndof | ux of A [x $10^{-3}$] | uy of A [x $10^{-3}$] |
| 319 | 832 P1-P1 | -0.3401 | -14.43 |
| | 2936 P2-P2 | -0.460 | -16.78 |
| | 6316 P3-P3 | -0.461 | -16.79 |
| 1365 | 3140 P1-P1 | -0.414 | -15.93 |
| | 11736 P2-P2 | -0.461 | -16.81 |
| | 25792 P3-P3 | -0.461 | -16.82 |
| 5143 | 11084 P1-P1 | -0.449 | -16.60 |
| | 42736 P2-P2 | -0.461 | -16.82 |
| | 94960 P3-P3 | -0.462 | -16.82 |
| Reference | | -0.469 | -16.97 |
| Error | | 1.49% | 0.88 % |

Table 1.7: CSM-2, deformation components of A(t) for $\Delta t = 0.05$ and increasing spatial refinement. The error is computed as the relative error from the highest mesh resolution against the reference solution.

| $\Delta t = 0.01$ $\theta = 0.5$ | | | |
|---|---|---|---|
| nel | ndof | ux of A [x $10^{-3}$] | uy of A [x $10^{-3}$] |
| 319 | 832 P1-P1 | -10.835 +/- 10.836 | -55.197 +/- 56.845 |
| | 2936 P2-P2 | -14.390 +/- 14.392 | -63.303 +/- 65.149 |
| | 6316 P3-P3 | -14.432 +/- 14.435 | -63.397 +/- 65.263 |
| 1365 | 3140 P1-P1 | -13.053 +/- 13.054 | -60.367 +/- 62.241 |
| | 11736 P2-P2 | -14.428 +/- 14.432 | -63.388 +/- 65.256 |
| | 25792 P3-P3 | -14.444 +/- 14.446 | -63.432 +/- 65.287 |
| 5143 | 11084 P1-P1 | -14.082 +/- 14.084 | -62.656 +/- 64.495 |
| | 42736 P2-P2 | -14.444 +/- 14.447 | -63.435 +/- 65.288 |
| | 94960 P3-P3 | -14.449 +/- 14.452 | -63.449 +/- 65.296 |
| Reference | | -14.305 +- -14.305 | -63.607 +- 65.160 |
| Error | | 1% ± 1% | 0.24% ± 0.24% |

Table 1.8: CSM-3, deformation components of A(t) for $\Delta t = 0.01$, with increasing temporal refinement. The error is computed as the relative error from the highest mesh resolution.

| $\Delta t = 0.005$ $\theta = 0.5$ | | | |
|---|---|---|---|
| nel | ndof | ux of A [x $10^{-3}$] | uy of A [x $10^{-3}$] |
| 319 | 832 P1-P1 | -10.846 +/- 10.848 | -56.049 +/- 56.053 |
| | 2936 P2-P2 | -14.390 +/- 14.391 | -63.738 +/- 64.703 |
| | 6316 P3-P3 | -14.429 +/- 14.430 | -63.833 +/- 64.810 |
| 1365 | 3140 P1-P1 | -13.057 +/- 13.057 | -60.813 +/- 61.826 |
| | 11736 P2-P2 | -14.426 +/- 14.427 | -63.827 +/- 64.801 |
| | 25792 P3-P3 | -14.440 +/- 14.441 | -63.854 +/- 64.845 |
| 5143 | 11084 P1-P1 | -14.091 +/- 14.091 | -63.195 +/- 63.981 |
| | 42736 P2-P2 | -14.441 +/- 14.441 | -63.856 +/- 64.847 |
| | 94960 P3-P3 | -14.446 +/- 14.446 | -63.865 +/- 64.860 |
| Reference | | -14.305 +- -14.305 | -63.607 +- 65.160 |
| Error | | 1% ± 1% | 0.4% ± 0.4% |

Table 1.9: CSM-3, deformation components of A(t) for $\Delta t = 0.005$, with increasing temporal refinement. The error is computed as the relative error from the highest mesh resolution.

(a) $t = 0$ (b) $t = 0.22$ (c) $t = 0.45$

Figure 1.4: CSM-3, visualization of deformation of the elastic flag for three time steps: (a) initial configuration, (b) half way extenstion, (c) full extension

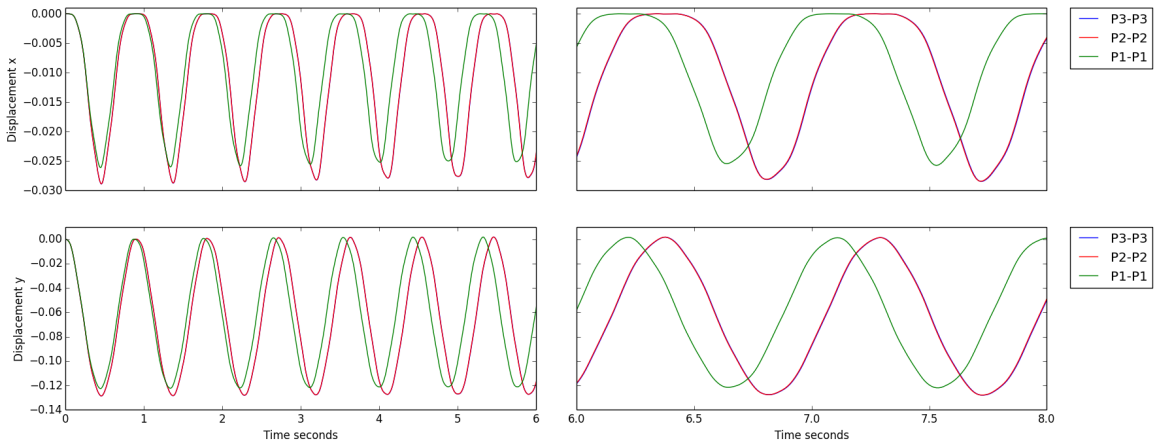


Figure 1.5: CSM-3 $\Delta t = 0.01$, deformation components of A(t) with finest mesh resolution, comparing all finite element pairs for time interval $t \in [0, 6]$ and $t \in [6, 8]$.

### Discussion

For CSM-1, the relative error of deformation found in Table 4.6, is 1.41% and 0.8% for the x and y coordinate respectively. In Table 4.7, a relative error of 1.49% and 0.88% for the x,y components can be found for CSM-2, proving both steady state problems coincide with the reference solution. In Table 4.8, the numerical solutions CSM-3 for time steps $\Delta t = 0.01$ and $\Delta t = 0.005$, are in close resemblance with the reference solution. The study of lower-order elements proved successful for all problems, justifying accurate results can be achieved by P2-P2 elements for deformation and velocity, even for coarse mesh resolution. Comparing all finite-element pairs for CSM-3, visualized in figure 4.5, shows P2-P2 and P3-P3 elements hardly can be distinguished from each other. By the previous mentioned results and observations, the solid solver is validated in accordance with the validation benchmark.

### 1.2.3 Validation of fluid structure interaction solver

The validation of the FSI solver consist of three sub-problems which will be referred to FSI-1, FSI-2 and FSI-3. The FSI-1 problem yields a steady state solution for the system, inducing small deformations to the elastic flag. The FSI-2 and FSI-3 problems results in a periodic solution, where the elastic flag oscillates behind the cylinder. All sub-problems inherit the conditions from the previous validation branches, with the exception of no gravitational force on the elastic frag On the fluid-structure interface $\Gamma$, we enforce the kinematic and dynamic boundary condition

$$\mathbf{v}_f = \mathbf{v}_s \tag{1.3}$$

$$\sigma_f \cdot \mathbf{n} = \sigma_s \cdot \mathbf{n} \tag{1.4}$$

Apart from the accuracy of the reported values, the main purpose of the validation of the solver is twofold. First, it is of great importance to ensure that the overall coupling of the fluid-structure interaction problem is executed correctly. Second, a good choice of mesh extrapolation model is essential to ensure that mesh entanglement is not present. Based on experience in section, 4.2.1-2, the finite element pair P2-P1 for the fluid solver, and P2-P2 for the solid solver proved successful. Therefore the finite-elements P2-P2-P1 for deformation, velocity, and pressure are chosen for the numerical experiments. Higher order elements will not be examined, mainly due to long computational time, even for optimized solver approaches.

| Solid parameters | | | |
|---|---|---|---|
| parameter | FSI-1 | FSI-2 | FSI-3 |
| $\rho^s[10^3 \frac{kg}{m^3}]$ | 1 | 10 | 1 |
| $\nu^s$ | 0.4 | 0.4 | 0.4 |
| $\mu^s[10^6 \frac{kg}{ms^2}]$ | 0.5 | 0.5 | 2.0 |
| Fluid parameters | | | |
| $\rho^f[10^3 \frac{kg}{m^3}]$ | 1 | 1 | 1 |
| $\nu^f[10^{-3} \frac{m^2}{s}]$ | 1 | 1 | 1 |
| U | 0.2 | 1 | 2 |
| parameter | FSI-1 | FSI-2 | FSI-3 |
| Re | 20 | 100 | 200 |

Table 1.10: Fluid-structure interaction sub-problem parameters

**Results**

The numerical results for FSI-1, FSI-2, and FSI-3 are shown in Table 4.10-12. For all sub-problems, a spatial convergence study has been conducted on three different meshes with increasing resolution, with the relative error of the finest spatial and temporal resolution. For FSI-1 in Table 4.10, an additional option is proposed, omitting mesh moving models from the monolithic variational form from section 3.2.2. A comparison of the validation parameters lift, drag, and displacement with different mesh moving models can be found in Figure 4.2-3. Finally, Figure 4.7 and 4.9 visualize the flow field and deformation of the elastic flag for a given time,

**FSI-1**

| Laplace | | | | | |
|---|---|---|---|---|---|
| nel | ndof | ux of A [x $10^{-3}$] | uy of A [x $10^{-3}$] | Drag | Lift |
| 2474 | 21249 | 0.0226 | 0.8200 | 14.061 | 0.7542 |
| 7307 | 63365 | 0.0227 | 0.7760 | 14.111 | 0.7517 |
| 11556 | 99810 | 0.0226 | 0.8220 | 14.201 | 0.7609 |
| Reference | | 0.0227 | 0.8209 | 14.295 | 0.7638 |
| Error | | 0.0 % | 0.0 % | 0.66 % | 0.38 % |
| Linear Elastic | | | | | |
| nel | ndof | ux of A [x $10^{-3}$] | uy of A [x $10^{-3}$] | Drag | Lift |
| 2474 | 21249 | 0.0226 | 0.8198 | 14.061 | 0.7541 |
| 7307 | 63365 | 0.0227 | 0.7762 | 14.111 | 0.751 |
| 11556 | 99810 | 0.0226 | 0.8222 | 14.201 | 0.7609 |
| Reference | | 0.0227 | 0.8209 | 14.295 | 0.7638 |
| Error | | 0.0 % | 0.0 % | 0.66 % | 0.38 % |
| Biharmonic bc1 | | | | | |
| nel | ndof | ux of A [x $10^{-3}$] | uy of A [x $10^{-3}$] | Drag | Lift |
| 2474 | 21249 | 0.0226 | 0.8200 | 14.061 | 0.7541 |
| 7307 | 63365 | 0.0227 | 0.7761 | 14.111 | 0.7517 |
| 11556 | 99810 | 0.0227 | 0.8017 | 14.205 | 0.9248 |
| Reference | | 0.0227 | 0.8209 | 14.295 | 0.7638 |
| Error | | 0.0 % | 0.0 % | 0.63 % | 21.08 % |
| Biharmonic bc2 | | | | | |
| nel | ndof | ux of A [x $10^{-3}$] | uy of A [x $10^{-3}$] | Drag | Lift |
| 2474 | 21249 | 0.0226 | 0.8200 | 14.061 | 0.7543 |
| 7307 | 63365 | 0.0227 | 0.7761 | 14.111 | 0.7518 |
| 11556 | 99810 | 0.0227 | 0.8020 | 14.205 | 0.9249 |
| Reference | | 0.0227 | 0.8209 | 14.295 | 0.7638 |
| Error | | 0.0 % | 0.0 % | 0.63 % | 21.09 % |
| No extrapolation | | | | | |
| nel | ndof | ux of A [x $10^{-3}$] | uy of A [x $10^{-3}$] | Drag | Lift |
| 2474 | 21249 | 0.0224 | 0.9008 | 14.064 | 0.7713 |
| 7307 | 63365 | 0.0226 | 0.8221 | 14.117 | 0.7660 |
| 11556 | 99810 | 0.0225 | 0.8787 | 14.212 | 0.7837 |
| Reference | | 0.0227 | 0.8209 | 14.295 | 0.7638 |
| Error | | 0.0 % | 0.0 % | 0.58 % | 2.61 % |

Table 1.11: FSI 1 - Comparison of mesh extrapolation models for three spatial refinements

**FSI-2**

| Laplace $\Delta t = 0.01$ $\theta = 0.51$ | | | | | |
|---|---|---|---|---|---|
| nel | ndof | ux of A [x $10^{-3}$] | uy of A [x $10^{-3}$] | Drag | Lift |
| 2474 | 21249 | -15.27 ± 13.45 | 1.34 ± 82.4 | 157.00 ±14.85 | -1.09 ±258.47 |
| 7307 | 63365 | -14.23 ±13.37 | 1.31 ± 82.2 | 159,3 ± 15.43 | 0.92± 254.53 |
| 11556 | 99810 | -14.96 ± 13.24 | 1.28 ± 81.9 | 161.07 ± 17.81 | 0.02 ± 256.04 |
| $\Delta t = 0.001$ $\theta = 0.5$ | | | | | |
| nel | ndof | ux of A [x $10^{-3}$] | uy of A [x $10^{-3}$] | Drag | Lift |
| 2474 | 21249 | -15.61± 13.21 | 1.34 ± 83.6 | 155.38 ± 13.98 | -3.00 ± 289.06 |
| 7307 | 63365 | -15.31 ± 13.07 | 1.02 ± 82.8 | 156.81 ± 14.95 | -2.00 ± 276.24 |
| 11556 | 99810 | -15.28 ± 13.04 | 1.28 ± 82.9 | 158.45 ± 16.09 | -2.53 ± 276.13 |
| Reference | | -14.58 ± 12.44 | 1.23 ±80.6 | 208.83 ± 73.75 | 0.88 ± 234.2 |
| Error | | 0.0% ± 0.0 % | 0.0 % ± 0.0 % | 24.1 % ± 78.1 % | 387.5 % ± 17.9 % |

| Biharmonic 1 $\Delta t = 0.01$ $\theta = 0.51$ | | | | | |
|---|---|---|---|---|---|
| nel | ndof | ux of A [x $10^{-3}$] | uy of A [x $10^{-3}$] | Drag | Lift |
| 2474 | 21249 | -15.44 ± 13.24 | -1.38 ± 82.3 | 157.67 ± 15.02 | -0.89± 258.87 |
| 7307 | 63365 | -15.04 ± 12.96 | 0.99 ± 81.9 | 159.83± 16.83 | 0.98 ± 245.40 |
| 11556 | 99810 | -15.29± 13.17 | 1.29 ± 82.5 | 161.69 ± 18.73 | -1.86 ± 251.30 |
| $\Delta t = 0.001$ $\theta = 0.5$ | | | | | |
| nel | ndof | ux of A [x $10^{-3}$] | uy of A [x $10^{-3}$] | Drag | Lift |
| 2474 | 21249 | -15.36 ± 13.12 | 1.35 ± 83.1 | 155.38 ± 13.74 | -2.55 ± 285.19 |
| 7307 | 63365 | -15.23 ± 12.97 | 1.03± 82.4 | 157.14 ± 15.18 | -8.62 ± 263.87 |
| 11556 | 99810 | -15.27 ± 12.99 | 1.31 ± 82.7 | 157.72 ± 15.58 | 3.34 ± 258.76 |
| Reference | | -14.58 ± 12.44 | 1.23 ±80.6 | 208.83 ± 73.75 | 0.88 ± 234.2 |
| Error | | 0.0% ± 0.0 % | 0.0 % ± 0.0 % | 24.4% ± 78.8 % | 279.5 % ± 10.4 % |

| Biharmonic 2 $\Delta t = 0.01$ $\theta = 0.51$ | | | | | |
|---|---|---|---|---|---|
| nel | ndof | ux of A [x $10^{-3}$] | uy of A [x $10^{-3}$] | Drag | Lift |
| 2474 | 21249 | -14.93 ± 13.22 | 1.35 ± 81.5 | 157.76 ± 15.04 | -0.49 ± 254.13 |
| 7307 | 63365 | -14.67± 13.05 | 1.00± 80.9 | 159.59 ± 16.77 | 2.22 ± 248.11 |
| 11556 | 99810 | 1.58 ± 12.86 | 1.23± 81.5 | 161.85 ±18.84 | -1.64 ± 247.04 |
| $\Delta t = 0.001$ $\theta = 0.5$ | | | | | |
| nel | ndof | ux of A [x $10^{-3}$] | uy of A [x $10^{-3}$] | Drag | Lift |
| 2474 | 21249 | -15.63 ± 12.7 | 1.31 ± 82.9 | 155.55 ± 13.82 | -2.45 ± 281.18 |
| 7307 | 63365 | -14,99 ± 12.81 | 0.99± 82.14 | 156.86 ± 15.05 | -1.65 ± 269.84 |
| 11556 | 99810 | -15.26 ± 12.91 | 1.27 ± 81.8 | 156.86 ± 15.05 | -1.65 ± 269.84 |
| Reference | | -14.58 ± 12.44 | 1.23 ±80.6 | 208.83 ± 73.75 | 0.88 ± 234.2 |
| Error | | 0.0 % ± 0.0 % | 0.0 % ± 0.0 % | 24.8 % ± 79.5 % | 287.5 % ± 15.2 % |

Table 1.12: FSI 1 - Comparison of mesh extrapolation models for $\Delta t = [0,01, 0,001]$, for three spatial refinements

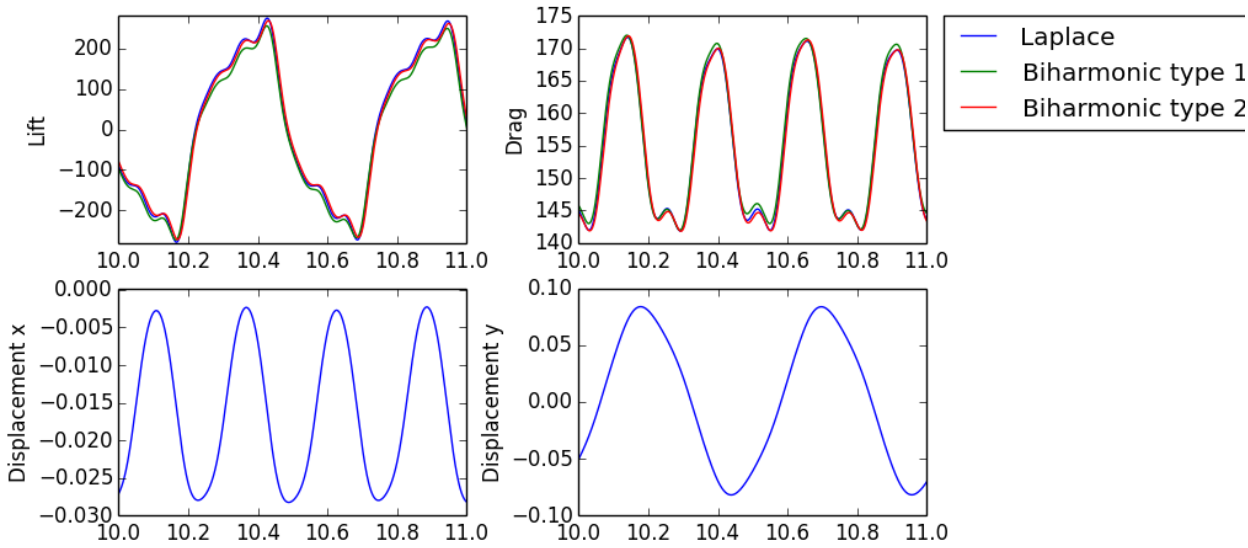


Figure 1.6: FSI-2, visualization of fully developted flow with structure deformation at time t = 9s.

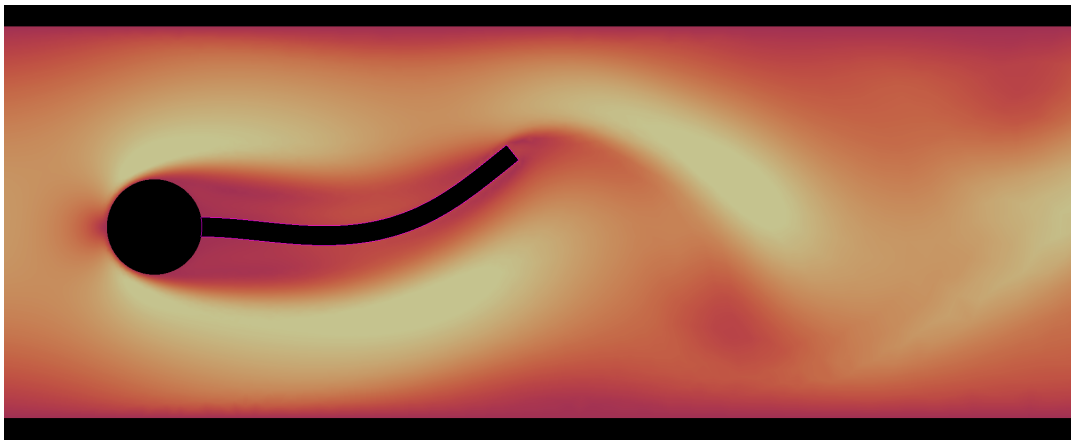

Figure 1.7: FSI-2, visualization of fully developted flow with structure deformation at time t = 9s.

**FSI-3**

Table 1.13: FSI 3 - Comparison of mesh extrapolation models

| Laplace $\Delta t = 0.01 \theta = 0.51$ | | | | | |
|---|---|---|---|---|---|
| nel | ndof | ux of A [x $10^{-3}$] | uy of A [x $10^{-3}$] | Drag | Lift |
| 2474 | 21249 | -2.41 ± 2.41 | 1.49 ± 32.21 | 449.39 ± 14.72 | 0.55 ± 155.80 |
| 7307 | 63365 | -2.32 ± 2.31 | 1.32 ± 31.80 | 451.76 ± 16.10 | 1.04 ± 151.51 |
| 11556 | 99810 | -2.34 ± 2.34 | 1.59 ± 31.91 | 455.94 ± 17.34 | -0.01 ± 151.36 |
| $\Delta t = 0.001 \theta = 0.5$ | | | | | |
| nel | ndof | ux of A [x $10^{-3}$] | uy of A [x $10^{-3}$] | Drag | Lift |
| 2474 | 21249 | -2.91 ± 2.74 | 1.28 ± 35.01 | 450.90 ± 18.11 | 2.28 ±161.13 |
| 7307 | 63365 | -2.82 ± 2.66 | 1.24 ± 34.69 | 453.56 ± 19.80 | 2.94 ± 158.67 |
| 11556 | 99810 | -2.88 ± 2.72 | 1.49 ± 34.97 | 458.60 ± 22.12 | 2.23 ± 158.95 |
| Reference | | -2.69 ± 2.56 | 1.48 ± 34.38 | 457.3 ± 22.66 | 2.22 ± 149.78 |
| Error | | 0.0% ± 0.0 % | 0.0 % ± 0.0 % | 0.28 % ± 2.38 % | 0.45 % ± 6.12 % |

| Biharmonic 1 $\Delta t = 0.01 \theta = 0.51$ | | | | | |
|---|---|---|---|---|---|
| nel | ndof | ux of A [x $10^{-3}$] | uy of A [x $10^{-3}$] | Drag | Lift |
| 2474 | 21249 | -2.40 ± 2.38 | 1.58 ± 32.07 | 450.16 ± 15.11 | -20.09 ± 148.17 |
| 7307 | 63365 | -2.26 ± 2.14 | 1.70 ± 31.3 | 457.37 ± 15.24 | -51.77 ± 127.28 |
| 11556 | 99810 | -2.33 ± 2.32 | 1.93 ± 31.5 | 456.40 ± 17.45 | 0.45 ± 149.68 |
| $\Delta t = 0.001 \theta = 0.5$ | | | | | |
| nel | ndof | ux of A [x $10^{-3}$] | uy of A [x $10^{-3}$] | Drag | Lift |
| 2474 | 21249 | -2.18 ± 2.10 | 3.52 ± 2.90 | 435.19 ± 9.77 | -1.59± 151.45 |
| 7307 | 63365 | -2.80 ± 2.64 | 1.25 ± 3.45 | 454.38 ± 19.76 | 17.97 ± 155.08 |
| 11556 | 99810 | -2.84 ± 2.68 | 1.50 ± 3.47 | 459.12 ± 22.97 | -3.12 ± 171.22 |
| Reference | | -2.69 ± 2.56 | 1.48 ± 34.38 | 457.3 ± 22.66 | 2.22 ±- 149.78 |
| Error | | 0.0 % ± 0.0 % | 0.0 % ± 0.0 % | 0.40 % ± 1.37 % | 240.5 % ± 14.3 % |

| Biharmonic 2 $\Delta t = 0.01 \theta = 0.51$ | | | | | |
|---|---|---|---|---|---|
| nel | ndof | ux of A [x $10^{-3}$] | uy of A [x $10^{-3}$] | Drag | Lift |
| 2474 | 21249 | -2.33 ± 2.33 | 1.57 ± 31.6 | 449.44 ± 14.82 | 0.80 ±152.03 |
| 7307 | 63365 | -2.25 ± 2.23 | 1.35 ± 31.3 | 452.63 ±16.29 | 17.11 ± 146.05 |
| 11556 | 99810 | -2.25 ± 2.29 | 1.59 ± 31.4 | 457.89 ± 17.26 | 57.83 ± 141.69 |
| $\Delta t = 0.001 \theta = 0.5$ | | | | | |
| nel | ndof | ux of A [x $10^{-3}$] | uy of A [x $10^{-3}$] | Drag | Lift |
| 2474 | 21249 | -2.83 ± 2.66 | 1.31 ± 34.5 | 450.24 ± 18.25 | 2.57 ± 175.42 |
| 7307 | 63365 | -2.77 ± 2.61 | 0.98± 34.6 | 453.53 ± 20.01 | 2.60 ± 159.13 |
| 11556 | 99810 | -2.80 ± 2.65 | 1.37 ± 34.7 | 458.41 ± 22.23 | 15.56 ± 157.78 |
| Reference | | -2.69 ± 2.56 | 1.48 ± 34.38 | 457.3 ± 22.66 | 2.22 ±- 149.78 |
| Error | | 0.0% ± 0.0 % | 0.0% ± 0.0% | 0.24 % ± 1.90 % | 600.9 % ± 5.34 % |

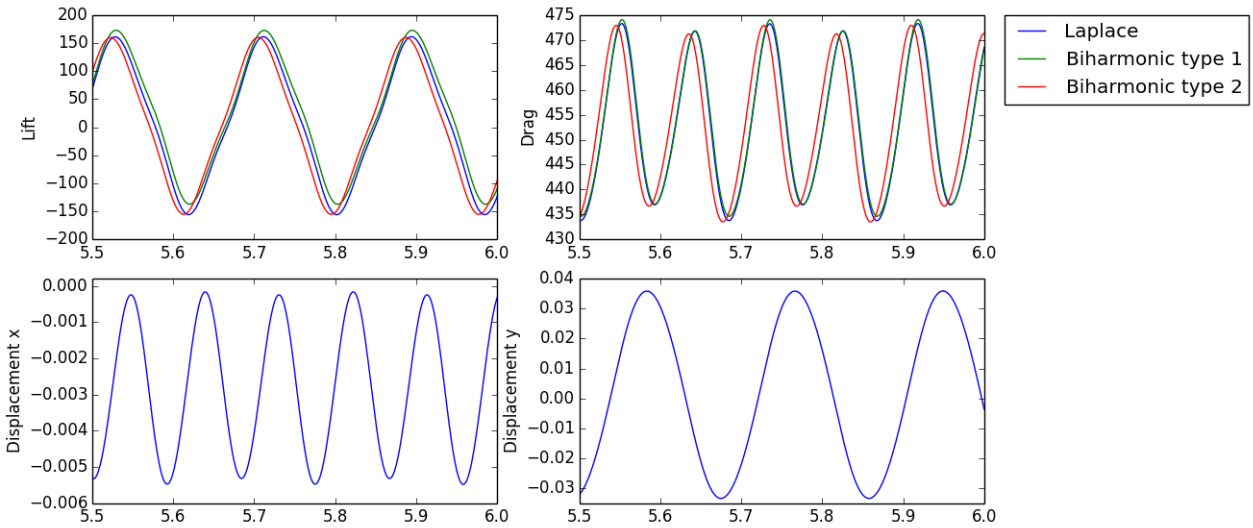


Figure 1.8: Comparison of mesh motion models for FSI-3, in time interval t $t \in [5.5, 6]$.

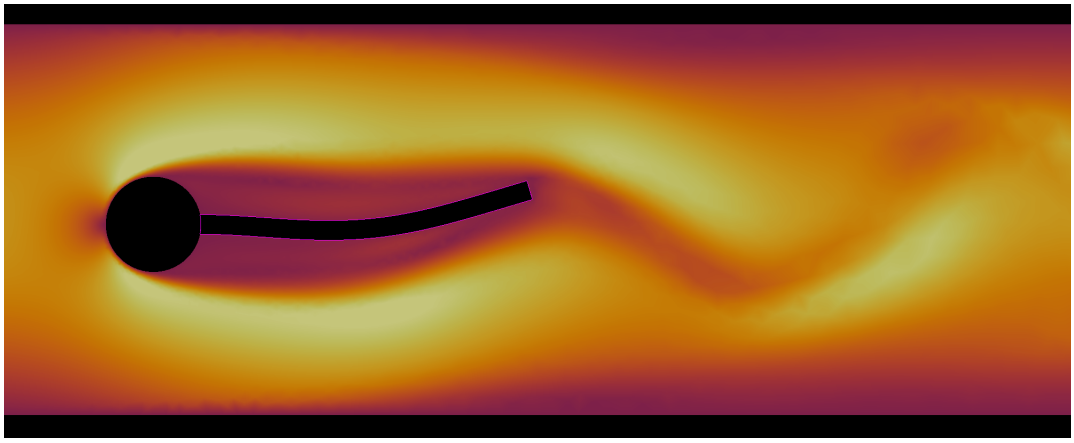

Figure 1.9: FSI-3, visualization of fully developted flow with structure deformation at time t = 5.1s.

### Discussion

For FSI-1, all models excel well in comparison with the reference solution, even at course mesh resolution. Due to low reynolds number flow the induced deformation of the elastic flag is very small, FSI-1 proves to be excellent for initial validation of fluid-structure interaction solvers. However, due the small deformations of the elastic flag of order $10^{-5}$, FSI-1 doesn't provide a rigorous test case for mesh extrapolation models. By omitting mesh extrapolation from the variatonal formulation in section 3.3.2, reasonable results are still obtained in Table 4.10. This fact proves FSI-1 to be misguiding in terms of mesh extrapolation model, but remains excellent for initial validation of fluid-structure interaction solvers and the overall coupling of the fluid and solid equations.

The FSI-2 problem proved to be one of the most demanding tests, due to the large deformation of the elastic flag. By the large deformation, the chance of fluid mesh entanglement was considerably high, stressing the mesh moving models extensively. The linear elastic model failed for both time sizes, but not due to mesh entanglement but early failure of the Newton-solver. This finding is comparable with the investigation conducted in [29], where early failure of the newton-solver is in context with long-term simulation of the implicit Crank-Nicholson scheme. In their study, a shifted implicit shifted Crank-Nicholson scheme $\theta = 0.5 + \Delta t$ proved to further improve stability for the newton-solver, making the numerical scheme stable for coarse time-step. Further, numerical investigation in [29] showed that for both Crank-Nicholson and shifted Crank-Nicholson are stable for $\Delta t < 0.003$ for the same benchmark. In my study, both implicit schemes was applicable for all mesh moving models, except the linear elastic model.

In general, the numerical solution regarding deformation of the elastic flag proved accurate in accordance with the reference solution for all sub-problems. However, the evaluation of drag and lift proved challenging for the periodic FSI-2 and FSI-3 problems. For FSI-2, poor accuracy was observed for all mesh resolutions and time steps, while for FSI-3 the evaluation of drag remained accurate. The same observations was found in [41], a followup work of the original benchmark [15], where numerical solutions committed by different research communities was compared. Here, both partitioned and monolithic solvers was compared. The diversity of lift and drag values provided by different research communities was surprising, as differences of order 50% for drag and lift values, and 10% for displacement was observed. More surprisingly was that the authors of the original benchmark [15], who also committed their numerical results, didn't match their own reference solution with the same solver. Therefore, comparison of lift and drag forces with the reference solution alone can be misleading, and should not be the main acceptance criteria for code validation for this benchmark. Given the remarks in [41], the comparison of deformation is arguably a better main acceptance criteria. On this basis, the FSI code is validated in accordance with the original benchmark.

# Numerical Experiments

## 2.1 Comparison of mesh moving models

Mesh moving models are essential for numerical stability of fluid-structure interaction solvers. If the fluid mesh doesn't conform with the solid deformation, the risk of mesh entanglement increases with the possibility of instabilities or breakdown of the solver. In general, mesh models have shown to be either robust concerning mesh entanglements at the cost of computational time, or computational efficient with less robustness [23]. However, computational efficiency has proven not only to be dependent of the complexity of model, but also the regularity of the fluid mesh, reducing Newton iterations needed per time step [47].
In this section we compare the mesh moving models from section 3.1.4. for the FSI-3 benchmark. As the linear elastic model was found not applicable in section 4.2.3, the laplace and biharmonic model will be considered. We will compare vertical displacement of the elastic flag, regularity of the fluid mesh, and number of Newton iterations per time step for all mesh moving models. A serial naive Newton solver is used, avoiding any effects of speed-up techniques which may effect Newton iterations (see section 6.3.3).

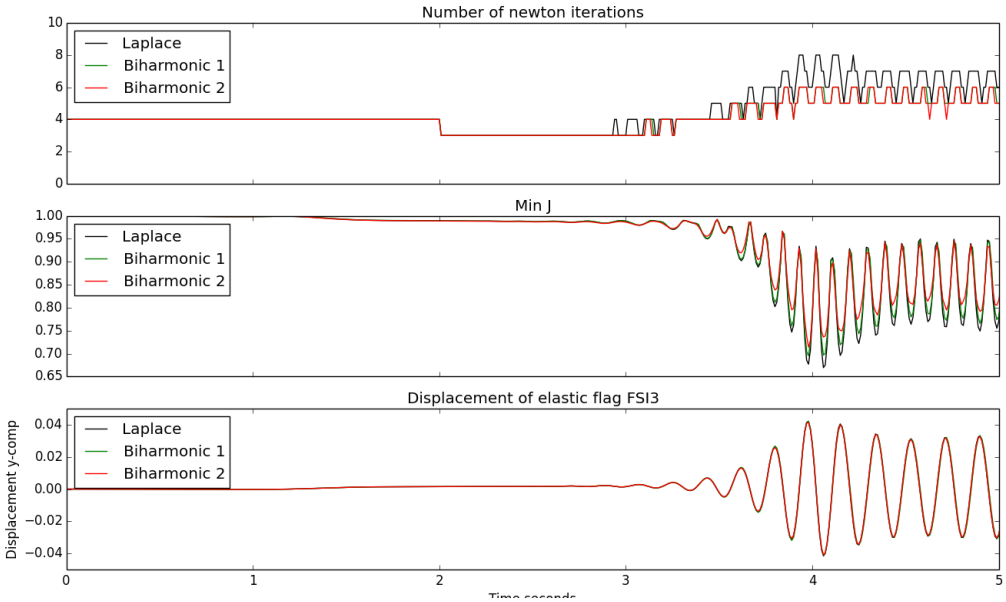


Figure 2.1: Investigation of mesh moving models for the FSI3 benchbark in the time interval $t \in [0, 5]$, comparing number of Newton iterations, mesh regularity, and vertical displacement of elastic flag

All mesh models seems to in Table 2.1

## 2.2 Investigation of temporal stability

One of the main challenges for constructing time-stepping schemes for ALE-methods, is the additional non-linearity introduced by the domain-velocity term in the fluid problem [9],

$$\hat{\mathrm{J}}_f(\hat{F}_f^{-1}(\hat{\mathbf{v}}_f - \frac{\partial \hat{\Gamma}_f}{\partial t}) \cdot \hat{\nabla})\hat{\mathbf{v}}_f \tag{2.1}$$

Closer inspection of the convection term reviles spatial and temporal differential operators depending non-linearly on one another. These differential operators often appear separated, making discretization of a general time-stepping scheme not directly intuitive. The domain-velocity $\frac{\partial \hat{\Gamma}_f}{\partial t}$ have proven to effect the stability of first and second-order time stepping schemes on fixed grids, but to what extent remains unclear [9, 8]. The second order Crank-Nicolson used in this thesis, have also shown to suffer from temporal stability for long-term simulations of fluid problems, on fixed-grids [46]. The unconditionally stable Crank-Nicolson scheme is restricted by the condition [46],

$$k \leq ch^{\frac{2}{3}} \tag{2.2}$$

*Where c is a costant, while k and h is the time-step and a mesh-size parameter*

while for the stability of the time derivative of the ALE-mapping, no accurate restriction is obtained (but thorough explored in [9]). As a result, time step restriction is necessary to ensure that numerical stability [9].

The temporal stability for the implicit Crank-Nicolson scheme, for the validation benchmark chosen in this thesis, was studied in [29]. The criteria for the numerical experiments was to obtain a stable solution in the time interval of 10 seconds, by temporal and spatial refinement studies. Following the ideas of [29], a second order scheme based on the Crank-Nicholson yields two possibilities.

**Discretization 2.1.** *Crank–Nicolson secant method*

$$\Big[\frac{\hat{\mathrm{J}}(\hat{\mathbf{u}}^n)\hat{\nabla}\hat{\mathbf{v}}^n\hat{\mathbf{F}}_W^{-1}}{2} + \frac{\hat{\mathrm{J}}(\hat{\mathbf{u}}^{n-1})\hat{\nabla}v^{n-1}\hat{\mathbf{F}}_W^{-1}}{2}\Big]\frac{\hat{\mathbf{u}}^n - \hat{\mathbf{u}}^{n-1}}{k}$$

**Discretization 2.2.** *Crank–Nicolson midpoint-tangent method*

$$\Big[\frac{\hat{\mathrm{J}}(\hat{\mathbf{u}}_{cn})\hat{\nabla}\hat{\mathbf{v}}_{cn}\hat{\mathbf{F}}_W^{-1}}{2}\Big]\frac{\hat{\mathbf{u}}^n - \hat{\mathbf{u}}^{n-1}}{k} \quad \hat{\mathbf{u}}_{cn} = \frac{\hat{\mathbf{u}}^n + \hat{\mathbf{u}}^{n-1}}{2} \;\; \hat{\mathbf{v}}_{cn} = \frac{\hat{\mathbf{v}}^n + \hat{\mathbf{v}}^{n-1}}{2}$$

The numerical experiments showed very similar performance for Discretization 2.1 and 2.2 , and significant differences of temporal accuracy was not found [29]. However, spatial and temporal refinement showed the implicit Crank-Nicolson scheme

gave stability problems for certain time-steps $k$. Choosing $k = [0.005, 0.003]$, the FSI-3 problem (Section 1.2.3) suffered from numerical instabilities. Interestingly, the instabilities occurred earlier in simulation time for increasing mesh refinement. A similar experiment in [48], showed reducing the time step $k = 0.001$ was necessary to yield stable long-time simulation for both Discretization 2.1 and 2.2

To coupe with the numerical unstabilities two approaches have been suggested in the litterature, the *shifted Crank-Nicolson* and the *frac-step method* [29, 48, 46],. In this thesis the shifted Crank-Nicolson scheme was considered, introducing stability to the overall system by shifting the $\theta$ parameter slightly to the implicit side. If the shift is dependent of the time-step $k$ such that $\frac{1}{2} \leq \theta \leq \frac{1}{2} + k$, the scheme will be of second order [29]. In the following section, we compare both Crank-Nicolson schemes suggested.

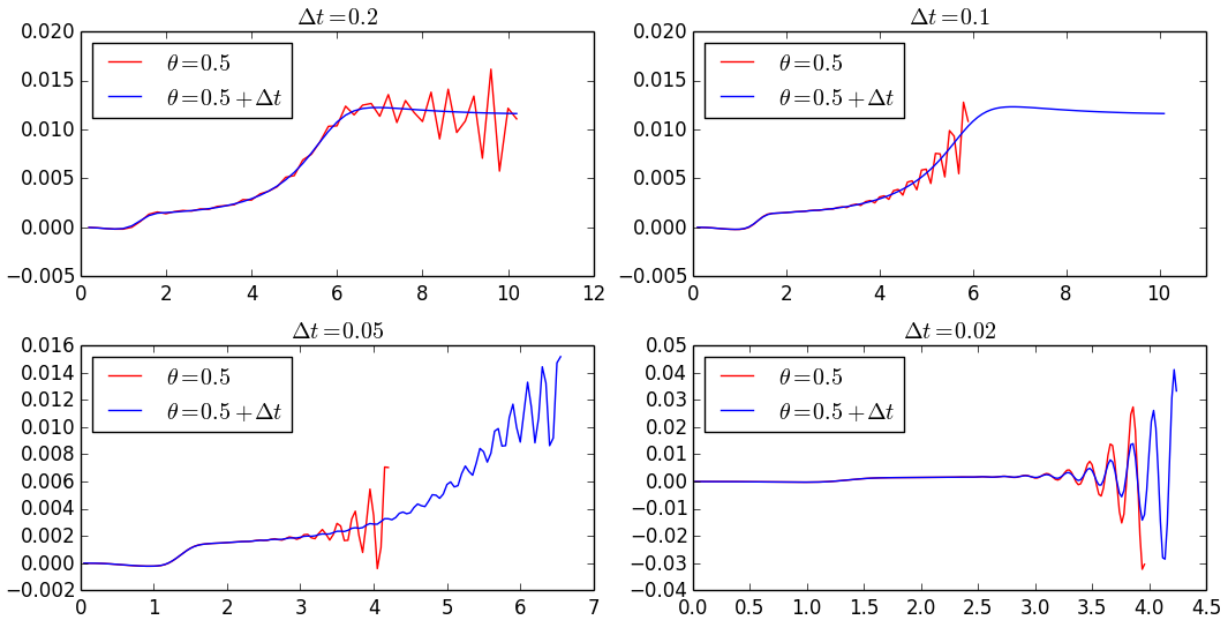


Figure 2.2: Investigation of temporal stability for the FSI3 benchbark in the time interval $t \in [0, 10]$, comparing the shifted crank nicolson to the original cranc nicolson scheme.

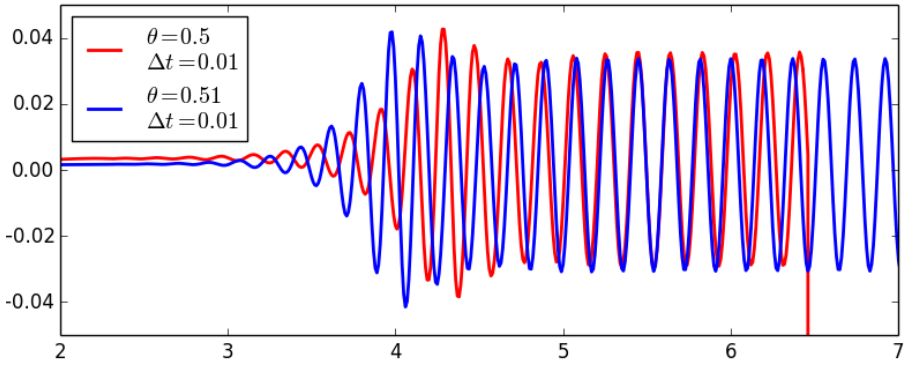


Figure 2.3: Investigation of temporal stability for the FSI3 benchbark in the time interval $t \in [0, 10]$, comparing the shifted crank nicolson to the original cranc nicolson scheme.

### Discussion

A numerical investigation of temporal stability in shown in Figure **??**, **??**„ where the shifted Crank-Nicolson scheme $\theta = 0.5 + k$, is compared the original Crank-Nicolson $\theta = 0.5$. The shifted version clearly show stability properties surpassing the original Crank-Nicolson scheme, for all numerical experiments. However, for $\Delta t \in [0.2, 0.1, 0.05, 0.02]$ the scheme clearly lacks the ability to capture the overall physics of the validation problem. Figure **??** showes long-time stability and expected physical behavior is obtained for $\Delta t = 0.01$. However, numerical experiments confirmed that $\Delta t \leq 0.001$ numerical stability was achieved regardless of both methods.

This result is important, reducing the overall computational time needed to achieve reasonable accuracy.

## 2.3 Optimization of Newtonsolver

A *bottleneck* express a phenomena where the total performance of a complete implementation is limited to small code fragments, accounting for the primary consumption of computer resources.
As for many other applications, within computational science one can often assume the consummation of resources follows the *The Pareto principle*. Meaning that for different types of events, roughly 80% of the effects come from 20% of the causes. An analogy to computational sciences it that 80% of the computational demanding operations comes from 20% of the code. In our case, the bottleneck is the newtonsolver. The two main reasons for this is

- **Jacobian assembly**
  The construction of the Jacobian matrix for the total residue of the system, is the most time demanding operations within the whole computation.

- **Solver**.
  As iterative solvers are limited for the solving of fluid-structure interaction problems, direct solvers was implemented for this thesis. As such, the operation of solving a linear problem at each iteration is computational demanding, leading to less computational efficient operations. Mention order of iterations?

Facing these problems, several attempts was made to speed-up the implementation. The FEniCS project consist of several nonlinear solver backends, were fully user-customization option are available. However one main problem which we met was the fact that FEniCS assembles the matrix of the different variables over the whole mesh, even though the variable is only defined in one to the sub-domains of the system.In our case the pressure is only defined within the fluid domain, and therefore the matrix for the total residual consisted of several zero columns within the structure region. FEniCS provides a solution for such problems, but therefore we were forced to construct our own solver and not make use of the built-in nonlinear solvers.

The main effort of speed-up were explored around the Jacobian assembly. Of the speed-ups methods explored in this thesis, some are *consistent* while others are *nonconsistent*. Consistent methods are methods that always will work, involving smarter approaches regarding the linear system to be solved. The non-consistent method presented involves altering the equation to be solved by some simplification of the system. As these simplifications will alter the expected convergence of the solver, one must take account for additional Newton iterations against cheaper Jacobi assembly. Therefore one also risk breakdown of the solver as the Newton iterations may not converge.

### 2.3.1 Consistent methods

#### Jacobi buffering

By inspection of the Jacobi matrix, some terms of the total residue is linear terms, and remain constant within each time step. By assembling these terms only in the

first Newton iteration will save some assembly time for the additional iterations needed each time step. As consequence the convergence of the Newton method should be unaffected as we do not alter the system.

### 2.3.2 Non-consisten methods

#### Reuse of Jacobian

As the assembly of the Jacobian at each iteration is costly, one approach of reusing the Jacobian for the linear system was proposed. In other words, the LU-factorization of the system is reused until the Jacobi is re-assembled. This method greatly reduced the computational time for each time step. By a user defined parameter, the number of iterations before a new assembly of the Jacobian matrix can be controlled.

#### Quadrature reduce

The assemble time of the Jacobian greatly depends on the degree of polynomials used in the discretisation of the total residual. Within FEniCS t he order of polynomials representing the Jacobian can be adjusted. The use of lower order polynomials reduces assemble time of the matrix at each newton-iteration, however it leads to an inexact Jacobian which may results to additional iterations.

### 2.3.3 Comparison of speedup methods

Table 2.1: Comparison of speedup techniques

| Laplace | | | | | |
|---|---|---|---|---|---|
| Implementation | Naive | Buffering | Reducequad. | Reusejacobi | Combined |
| Mean time/-timestep | 123.1 | | 31.4 | 61.3 | 11.1 |
| Speedup % | 1.0 | | 74.46% | 50.19% | 90.97 % |
| Mean iteration | 4.49 | | 10.1 | 10.2 | 10.2 |
| Biharmonic Type 1 | | | | | |
| Implementation | Naive | Buffering | Reducequad. | Reusejacobi | Combined |
| Mean time/-timestep | 243.3 | 307.6 | 51.6 | 76.7 | 24.8 |
| Speedup % | 1.0 | -26% | 78.7% | 68.4 % | 89.7% |
| Mean iteration | 4.1 | 6.2 | 4.6 | 7.1 | 6.8 |
| Biharmonic Type 2 | | | | | |
| Implementation | Naive | Buffering | Reducequad. | Reusejacobi | Combined |
| Mean time/-timestep | | | 60.5 | 95.3 | 20.7 |
| Speedup % | 1.0 | % | % | % | % |
| Mean iteration | 4.1 | | 6.29 | 6.9 | 6.9 |

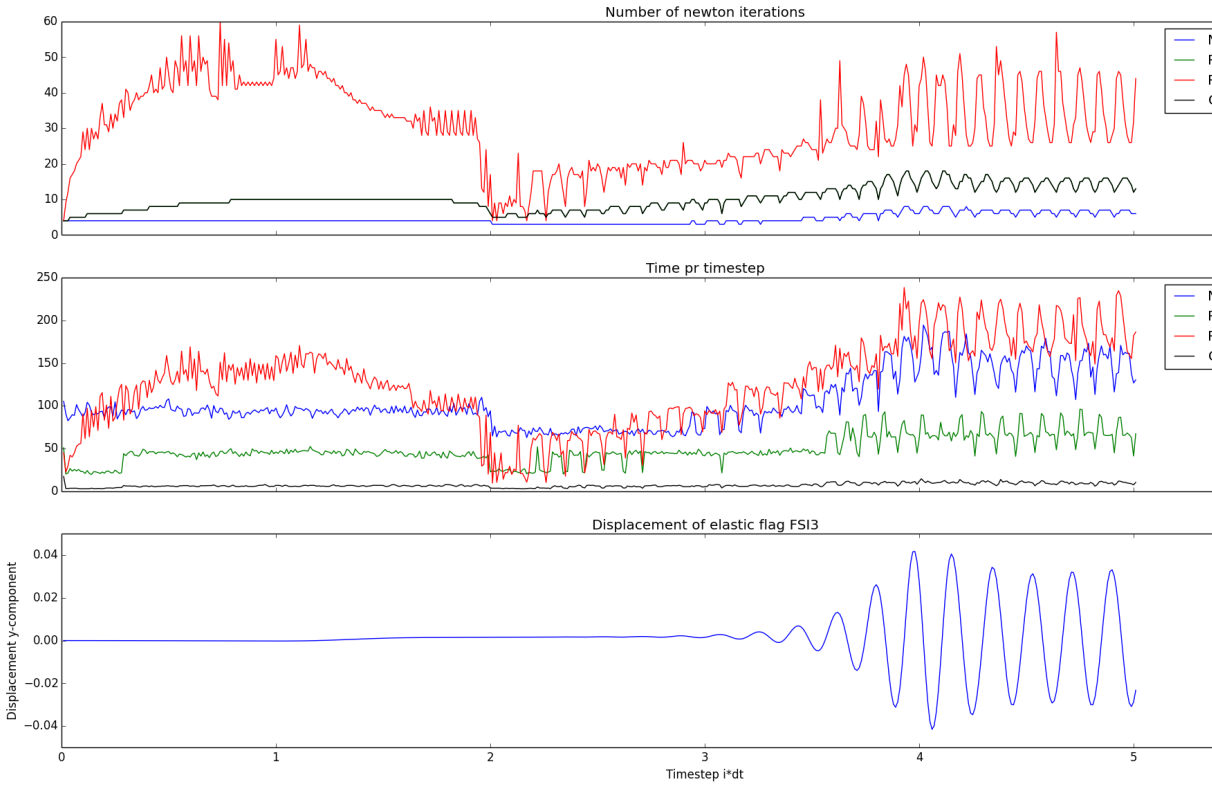


Figure 2.4: Comparison of speed-up techniques for the laplace mesh model

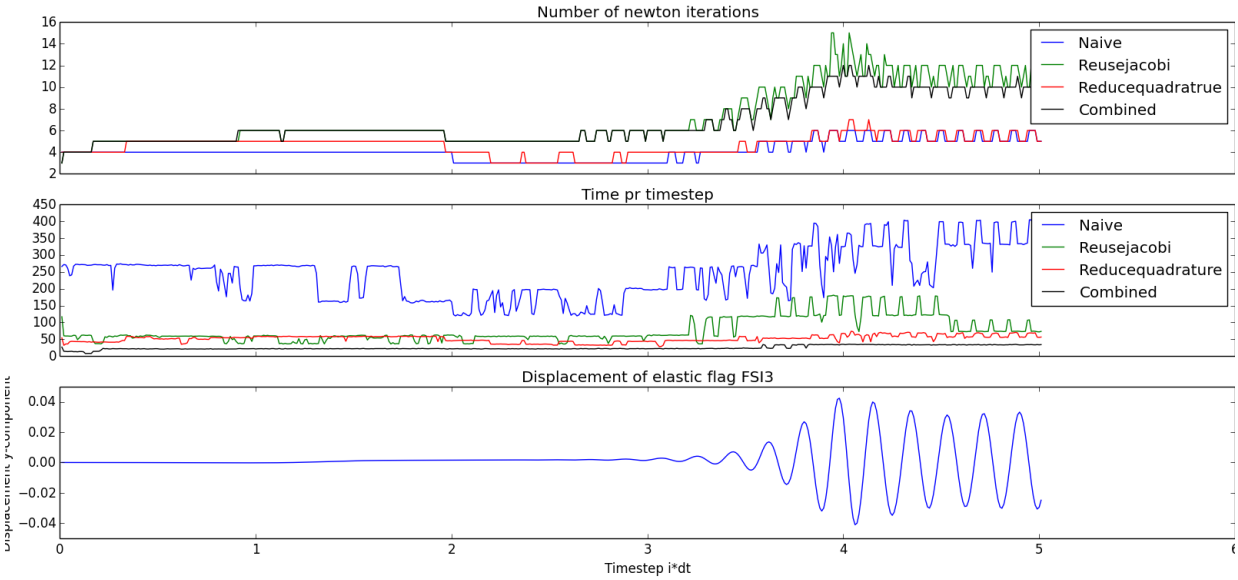


Figure 2.5: Comparison of speed-up techniques for the biharmonic type 1 mesh model

# Bibliography


[1] Robert T Biedron and Elizabeth M Lee-Rausch. Rotor Airloads Prediction Using Unstructured Meshes and Loose CFD/CSD Coupling.

[2] P I Crumpton. Implicit time accurate solutions on unstructured dynamic grids. (95):1–23, 1995.

[3] J Donea, A Huerta, J.-Ph Ponthot, and A Rodríguez-Ferran. Arbitrary Lagrangian-Eulerian methods. (1969):1–38, 2004.

[4] Richard P Dwight. Robust Mesh Deformation using the Linear Elasticity Equations.

[5] Stéphane Étienne, D Tremblay, and Dominique Pelletier. Code Verification and the Method of Manufactured Solutions for Fluid-Structure Interaction Problems. *36th AIAA Fluid Dynamics Conference and Exhibit*, (June):1–11, 2006.

[6] Miguel A Fernández and Jean-Frédéric Gerbeau. Algorithms for fluid-structure interaction problems. 2009.

[7] Miguel A. Fernández, Jean Frederic Gerbeau, and Ceremade Grandmont. A projection semi-implicit scheme for the coupling of an elastic structure with an incompressible fluid. *International Journal for Numerical Methods in Engineering*, 69(4):794–821, 2007.

[8] L Formaggia and F Nobile. A stability analysis for the arbitrary Lagrangian Eulerian formulation with finite elements. *East-west journal of numerical mathematics*, Vol. 7(No. 2):105–131, 1991.

[9] Luca Formaggia and Fabio Nobile. Stability analysis of second-order time accurate schemes for ALE-FEM. *Computer Methods in Applied Mechanics and Engineering*, 193(39-41 SPEC. ISS.):4097–4116, 2004.

[10] Christiane Förster, Wolfgang A. Wall, and Ekkehard Ramm. Artificial added mass instabilities in sequential staggered coupling of nonlinear structures and incompressible viscous flows. *Computer Methods in Applied Mechanics and Engineering*, 196(7):1278–1293, 2007.

[11] Bernhard Gatzhammer. Efficient and Flexible Partitioned Simulation of Fluid-Structure Interactions. page 261, 2014.

[12] Philippe Geuzaine. Numerical Simulations of Fluid-Structure Interaction Problems using MpCCI. (1):1–5.

[13] Brian T. Helenbrook. Mesh deformation using the biharmonic operator. *International Journal for Numerical Methods in Engineering*, 2003.

[14] Gerhard A. Holzapfel. *Nonlinear Solid Mechanics: A Continuum Approach for Engineering*. 2000.

[15] Jaroslav Hron and Stefan Turek. Proposal for numerical benchmarking of fluid-structure interaction between an elastic object and laminar incompressible flow. *Fluid-Structure Interaction*, 53:371–385, 2006.

[16] Ming-Chen Hsu and Yuri Bazilevs. Fluid–structure interaction modeling of wind turbines: simulating the full machine. *Computational Mechanics*, 50(6):821–833, dec 2012.

[17] Su-Yuen Hsu, Chau-Lyan Chang, and Jamshid Samareh. A Simplified Mesh Deformation Method Using Commercial Structural Analysis Software.

[18] Jay D. Humphrey. *Cardiovascular Solid Mechanics*. Springer New York, New York, NY, 2002.

[19] Hrvoje Jasak and Željko Tuković. Automatic mesh motion for the unstructured Finite Volume Method. *Transactions of Famena*, 30(2):1–20, 2006.

[20] Jae-Hyun Kim and Hyung-Cheol Shin. Application of the ALE technique for underwater explosion analysis of a submarine liquefied oxygen tank. *Ocean Engineering*, 35(8-9):812–822, jun 2008.

[21] V V Meleshko. Bending of an Elastic Rectangular Clamped Plate: Exact Versus 'Engineering' Solutions. *Journal of Elasticity*, 48(1):1–50, 1997.

[22] José Merodio and Giuseppe Saccomandi. Continuum Mechanics - Volume I. In *Volume 1*, chapter 3, pages 82–84. EOLSS, 2011.

[23] Selim MM and Koomullil RP. Mesh Deformation Approaches – A Survey. *Journal of Physical Mathematics*, 7(2), 2016.

[24] J Newman. *Marine Hydrodynamics*. 1977.

[25] William L. Oberkampf and Christopher J. Roy. *Verification and Validation in Scientific Computing*. Cambridge University Press, Cambridge, 2010.

[26] M Razzaq, Stefan Turek, Jaroslav Hron, J F Acker, F Weichert, I Grunwald, C Roth, M Wagner, and B Romeike. Numerical simulation and benchmarking of fluid-structure interaction with application to Hemodynamics. *Fundamental Trends in Fluid-Structure Interaction*, 1:171–199, 2010.

[27] T. Richter and T. Wick. Finite elements for fluid-structure interaction in ALE and fully Eulerian coordinates. *Computer Methods in Applied Mechanics and Engineering*, 199(41-44):2633–2642, 2010.

[28] Thomas Richter. Fluid Structure Interactions. 2016.

[29] Thomas Richter and Thomas Wick. On Time Discretizations of Fluid-Structure Interactions. pages 377–400. 2015.

[30] Patrick J. Roache. Code Verification by the Method of Manufactured Solutions. *Journal of Fluids Engineering*, 124(1):4, 2002.

[31] P.J. Roache. *Verification and Validation in Computational Science and Engineering*. Computing in Science Engineering, Hermosa Publishers, 1998, 8-9, 1998.

[32] Edward J. Rykiel. Testing ecological models: The meaning of validation. *Ecological Modelling*, 90(3):229–244, 1996.

[33] Kambiz Salari and Patrick Knupp. Code Verification by the Method of Manufactured Solution. Technical report, Sandia National Laboratories, 2000.

[34] LE Schwer. Guide for verification and validation in computational solid mechanics. *American Society of Mechanical Engineers*, PTC 60(V&V 10):1–15, 2006.

[35] Jason P Sheldon, Scott T Miller, and Jonathan S Pitt. Methodology for Comparing Coupling Algorithms for Fluid-Structure Interaction Problems. *World Journal of Mechanics*, 4(February):54–70, 2014.

[36] J.C. Simo and F. Armero. Unconditional stability and long-term behavior of transient algorithms for the incompressible Navier-Stokes and Euler equations. *Computer Methods in Applied Mechanics and Engineering*, 111(1-2):111–154, jan 1994.

[37] Ian Sommerville. Verification and Validation. Technical Report February, 2006.

[38] K Stein, T Tezduyar, and R Benney. Mesh Moving Techniques for Fluid-Structure Interactions With Large Displacements.

[39] Keith Stein, Richard Benney, Tayfun Tezduyar, and Jean Potvin. Fluid–structure interactions of a cross parachute: numerical simulation. *Computer Methods in Applied Mechanics and Engineering*, 191(6-7):673–687, dec 2001.

[40] Ryo Torii, Marie Oshima, Toshio Kobayashi, Kiyoshi Takagi, and Tayfun E. Tezduyar. Fluid–structure interaction modeling of a patient-specific cerebral aneurysm: influence of structural modeling. *Computational Mechanics*, 43(1):151–159, dec 2008.

[41] Stefan Turek, Jaroslav Hron, Mudassar Razzaq, and Hilmar Wobker. Numerical Benchmarking of Fluid-Structure Interaction : A comparison of different discretization and solution approaches.

[42] A V, T Passerini, A Quaini, U Villa, A Veneziani, and S Canic. Numerical Analysis and S cientific C omputing P reprint S eria Validation of an open source framework for the simulation of blood flow in rigid and deformable vessels P reprint # 17 D epartment of Mathematics University of Houston. 2013.

[43] Jan Vierendeels. Comparison of the Hemodynamic and Thrombogenic Performance of Two Bileaflet Mechanical Heart Valves Using a CFD/FSI Model. *Journal of Biomechanical Engineering*, 129(4):558, jan 2007.

[44] Wolfgang A. Wall, Axel , Gerstenberger, Peter , Gamnitzer, Christiane , Förster, and Ekkehard , Ramm. Large Deformation Fluid-Structure Interaction – Advances in ALE Methods and New Fixed Grid Approaches. In *Fluid-Structure Interaction: Modelling, Simulation, Optimisation*, pages 195—-232. Springer Berlin Heidelberg, 2006.

[45] Frank White. *Viscous fluid flow*. McGraw-Hill, third edit edition.

[46] T. Wick. Stability Estimates and Numerical Comparison of Second Order Time-Stepping Schemes for Fluid-Structure Interactions. In *Numerical Mathematics and Advanced Applications 2011*, pages 625–632. Springer Berlin Heidelberg, Berlin, Heidelberg, 2013.

[47] T Wick and Thomas Wick. Variational-monolithic ALE fluid-structure interaction: Comparison of computational cost and mesh regularity using different mesh motion techniques.

[48] Thomas Wick. *Adaptive Finite Element Simulation of Fluid-Structure Interaction with Application to Heart-Valve*. PhD thesis, Heidelberg.

[49] Thomas Wick. Solving Monolithic Fluid-Structure Interaction Problems in Arbitrary Lagrangian Eulerian Coordinates with the deal.II Library.

[50] Thomas Wick. Fluid-structure interactions using different mesh motion techniques. *Computers and Structures*, 89(13-14):1456–1467, 2011.

[51] Thomas Wick. Fully Eulerian fluid-structure interaction for time-dependent problems. *Computer Methods in Applied Mechanics and Engineering*, 255:14–26, 2013.

[52] Klaus Wolf, Schloss Birlinghoven, Code Coupling Interface, Open Programming Interface, and Distributed Simulation. Mpcci – the Generl Code Coupling Interface. *6. LS-DYNA Anwenderforum, Frankenthal 2007 IT*, pages 1–8, 2007.

[53] P. Wriggers. *Computational contact mechanics, second ed., Springer*. 2006.

[54] Hou Zhang, Xiaoli Zhang, Shanhong Ji, Yanhu Guo, Gustavo Ledezma, Nagi Elabbasi, and Hugues DeCougny. Recent development of fluid-structure interaction capabilities in the ADINA system. *Computers and Structures*, 81(8-11):1071–1085, 2003.